Chapter 3

Raypaths vs. Wavepaths

This chapter compares the ways rays and waves interrogate space by examining raypath and wavepath backprojection patterns in several domains. Because wavepaths ($\mathcal{L}_0$) are much less familiar than raypaths (L_0), the first section describes their physical characteristics in the frequency-space domain of wave-equation tomography's implementation. Rytov wavepaths are shown to best describe forward-scattered waves, transmitted through a velocity perturbation; Born wavepaths are shown to best describe back-scattered waves, reflected from a velocity perturbation. The second section summarizes the differences between raypaths and wavepaths in this domain and explains them in terms of the differing assumptions of ray and wave theory. The final section compares raypaths and wavepaths in the wavenumber domain.

3.1 Wavepaths: frequency-space domain

3.1.1 Homogeneous background velocity field

Figures 3.1a through 3.1e show Born and Rytov examples of two- and three-dimensional wavepaths for a homogeneous background velocity field. The velocity field is 2000 m/s; the sources and receivers are separated by 2000 m, and the familiar raypath analog is shown in Figure 3.1f. The patterns were generated analytically, using equations 2.8, 2.9, 2.12, and 2.16.

Unlike raypaths, wavepaths are monochromatic and complex. While the complex absolute values of the wavepaths decay with distance from the source and receiver (as $1/\sqrt{(\mathbf{g}-\mathbf{r})(\mathbf{s}-\mathbf{r})}$ in the 2-d case and as $1/(\mathbf{g}-\mathbf{r})(\mathbf{s}-\mathbf{r})$ in the 3-d case), the phase of

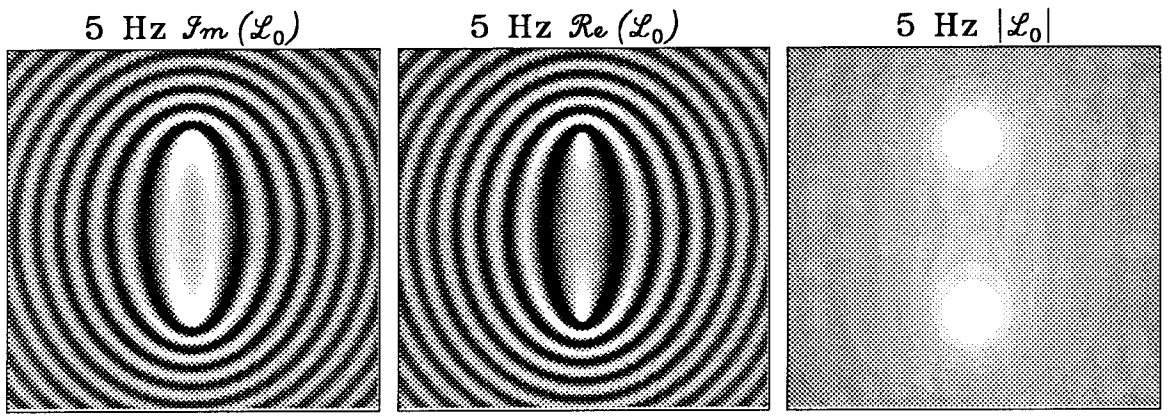

a) Rytov 2–D 5 Hz wavepath

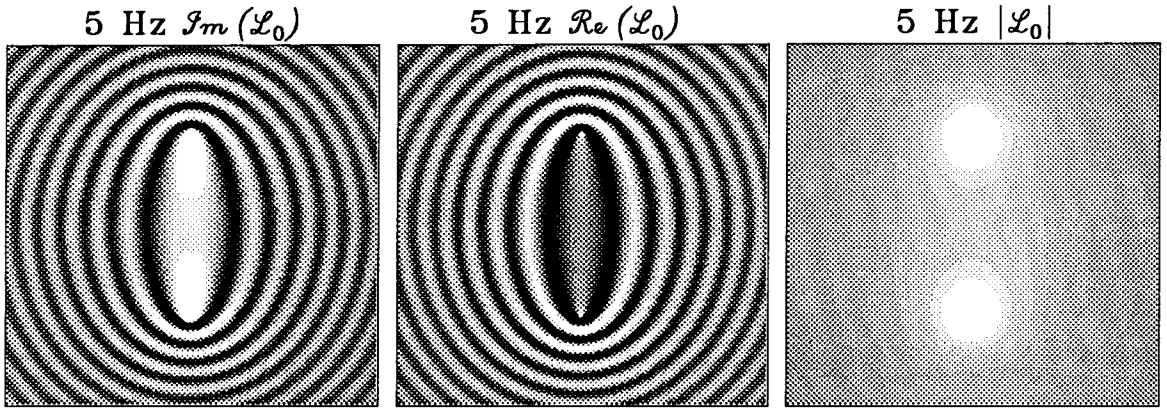

b) Born 2–D 5 Hz wavepath

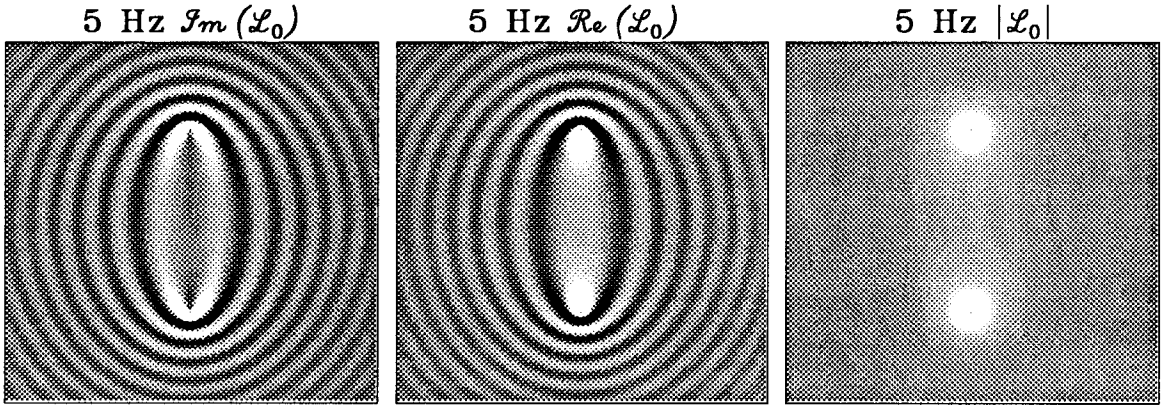

c) Rytov 3–D 5 Hz wavepath slice

FIG. 3.1. Frequency-space domain wavepaths for a constant-velocity background field. (a), (b) Two-dimensional Rytov and Born wavepaths ($\mathcal{L}_0$) for a 5 Hz source. (c) Slice through a three-dimensional, 5 Hz Rytov wavepath.

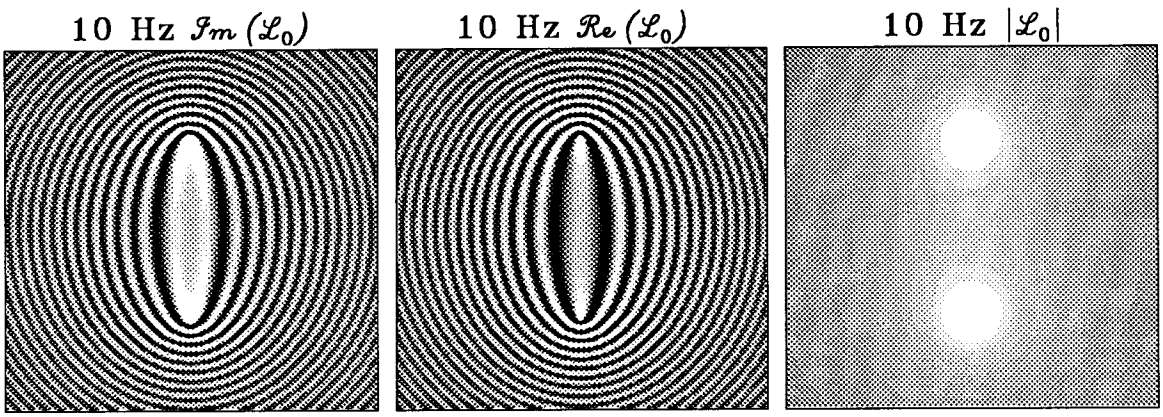

d) Rytov 2-D 10 Hz wavepath

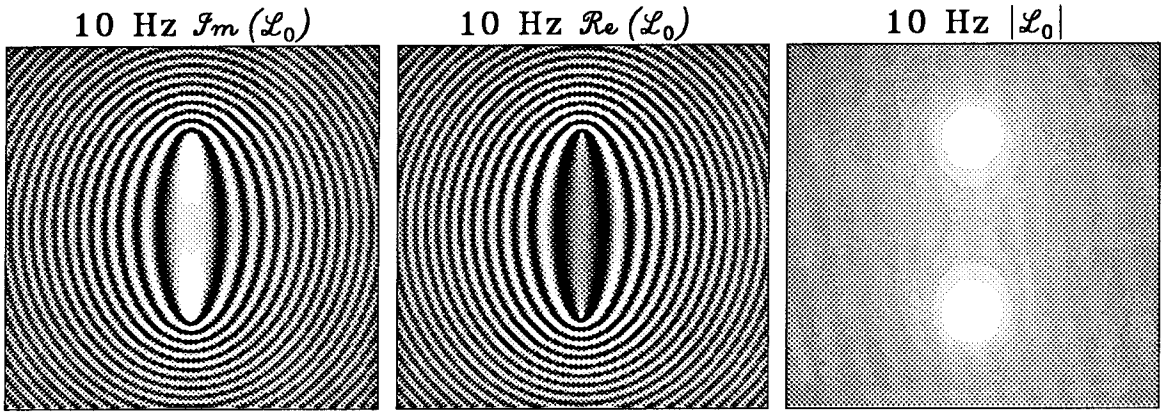

e) Born 2-D 10 Hz wavepath

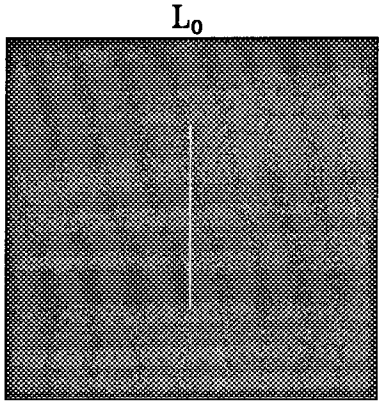

f) Raypath

FIG. 3.1. (contd.): (d), (e) Two-dimensional Rytov and Born wavepaths ($\mathcal{L}_0$) for a 10 Hz source. (f) The raypath (L_0) equivalent of $\mathcal{L}_0$.

the patterns oscillates from π to $-\pi$. Because the Born and Rytov approximations are based on scattering theory, contours of constant phase on the wavepaths yield confocal ellipses: curves of constant source-scatterer-receiver traveltimes, with the source and receiver located at the foci. The equation describing these ellipses is:

$$\frac{x^2}{a^2 - c^2} + \frac{z^2}{a^2} = 1; \quad a > c, \tag{3.1}$$

where a is the semimajor axis (half the scattering path from source to receiver) and c is half the source-receiver offset. The traveltime discrepancy between the direct source-receiver path (the equivalent raypath) and a scattered source-receiver path is $2(a - c)/v_0$. Beyond these observations, the fine structure of the wavepaths depends on whether they are Born- or Rytov-generated patterns.

Rytov

As described in chapter 2, the Rytov approximation creates a linear relation between velocity and complex-phase perturbations, causing phase and amplitude to separate naturally in the Rytov wavepath. When multiplied by $\Delta v/v$: the imaginary part of the wavepath yields the time-delay-like phase delay $\Delta\phi(\omega)$; the real part of the wavepath yields the log of the amplitude-ratio $\ln[A(\omega)/A_0(\omega)]$. This natural separation arises from the Rytov approximation's affinity for forward-scattered energy and transmission-geometry implementations of full-waveform inversion—where traveltime delays accumulate through a velocity perturbation. The strong parallelism between Rytov and ray-trace tomography results from the assumption $(\nabla(\Delta\Phi))^2 << {k_0}^2(1 - {v_0}^2/v^2)$ (or equivalently, $|\nabla \ln(A/A_0)/k_0| << 1$ and $|\nabla(\Delta\phi)/k_0| \leq 1$). By requiring both the amount of scattering per wavelength and the scattering angle to be small, these constraints are compatible with though less restrictive than transmission ray theory (Chernov, 1960) [1]. In fact, tomography under the Rytov and

[1]Chernov shows that small $|\nabla(\Delta\phi)|$ implies the change in the direction of gradient phase (the angle between initial and scattered energy) to be small in three lines:

$$\phi = \phi_0 + \Delta\phi = k_0 x + \Delta\phi(x, y, z)$$

$$\frac{\partial\phi}{\partial x} = k_0 + \frac{\partial\Delta\phi}{\partial x}; \qquad \frac{\partial\phi}{\partial y} = \frac{\partial\Delta\phi}{\partial y}; \qquad \frac{\partial\phi}{\partial z} = \frac{\partial\Delta\phi}{\partial z}$$

$$\left|\frac{\partial\phi}{\partial x}\right| \approx k_0; \qquad \left|\frac{\partial\phi}{\partial y}\right| << k_0; \qquad \left|\frac{\partial\phi}{\partial z}\right| << k_0.$$

eikonal approximations are equivalent in the very-short-wavelength limit (Devaney, 1981).

For both the two- and three-dimensional Rytov wavepaths, the imaginary parts of the patterns pass through zeroes at the boundaries between the first, second, third, etc. Fresnel zones. This structure identifies the innermost oscillation of the Rytov wavepaths with Hagedoorn's definition of a beam. Since a scatterer within the first Fresnel zone generates a wavefield reaching the geophone within a half wavelength of the source wavefield, a low velocity scatterer in this zone produces a phase delay—a high velocity scatterer a phase advance. Rytov wavepaths extend beyond Hagedoorn's beams because they work with monochromatic data, considering the full waveform instead of the first half wavelength. A scatterer in the second Fresnel zone generates a wavefield reaching the geophone between a half and a full wavelength behind the source wavefield: a low velocity scatterer produces a phase advance, a high velocity scatterer a phase delay. Similar arguments about phase explain the oscillations corresponding to the higher-numbered Fresnel zones; similar arguments about amplitudes explain the oscillations of the real parts of the Rytov wavepaths.

For the imaginary, three-dimensional wavepath slice in Figure 3.1c, there is an additional zero on the source-receiver Fermat path. Since a point on this curve scatters energy in phase with the background wavefield, it yields an amplitude perturbation but no phase perturbation at the receiver.

Born

Because the Born approximation creates a linear relation between velocity and complex-amplitude perturbations, phase and amplitude fail to separate in the Born wavepath. When multiplied by the object function, the real part of the Born wavepath yields $\Re[\Psi(\omega) - \Psi_0(\omega)]$, the imaginary part $\Im[\Psi(\omega) - \Psi_0(\omega)]$. This lack of correspondence between Born and transmission-style ray-trace tomography means Hagedoorn's beams cannot be found in Born wavepaths. Without the Rytov wavepaths' normalization factor of $G_0(\mathbf{s} - \mathbf{g})$, Born-wavepath zero crossings shift in a complex way with source-receiver separation and frequency. The imaginary 5 and 10 Hz patterns illustrated in Figures 3.1b and 3.1e are the same sign in the center only because their (wavelength)/(source-receiver separation) ratios are integer multiples of each other.

Born wavepaths are more naturally examined in the time-space domain of prestack migration. Figure 3.2 shows constant-velocity wavepaths in this domain, for three different

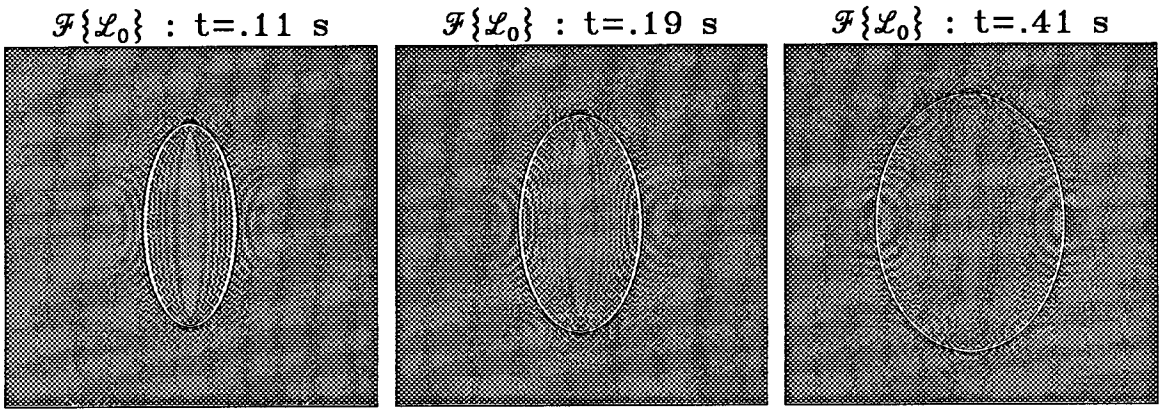

FIG. 3.2. Time-space domain wavepaths ($\mathcal{F}\{\mathcal{L}_0\}$) for a constant-velocity background field.

time slices. The patterns are instantly recognizable as the ellipses over which time arrivals are smeared in prestack migration (Schneider, 1971). While Born and Rytov wavepaths look alike in this domain (except for a time shift), the Born data parameters are much more suited to time than the Rytov parameters. Since the Fourier transform of $\Delta\Psi(\omega)$ is just the difference between the measured and expected seismic traces, Born tomography implemented in time-space corresponds to the projection of unexpected time arrivals back over isochronal scattering ellipses (Miller et al., 1987). Rytov tomography implemented in time-space corresponds to the projection of the Fourier transform of complex-phase perturbations back over these same patterns—a much less intuitively meaningful operation. The affinity of the Born approximation for reflection-geometry implementations of full-waveform inversion—for backscattered energy—arises from its weak-scattering assumption $\Delta\Psi << \Psi_0$ (or equivalently, $|\Delta A/A_0| << 1$ and $|\Delta\phi| << 1$). By requiring both the total amount of scattering and the total change in phase to be small, the method trades the ability to handle large cumulative phase delays for the ability to handle large scattering angles (Chernov, 1960).

3.1.2 Inhomogeneous background velocity field

Figures 3.3, 3.4 and 3.5 show examples of wavepaths in inhomogeneous media: for refraction through a vertical gradient; for transmission through layers, and for reflection above an interface. Because analytical solutions for Green's functions in these media are not readily available, they were calculated numerically. For each case a data cube, $d(x,z,t)$, was generated by two-dimensional finite-difference modeling, then Fourier transformed over time.

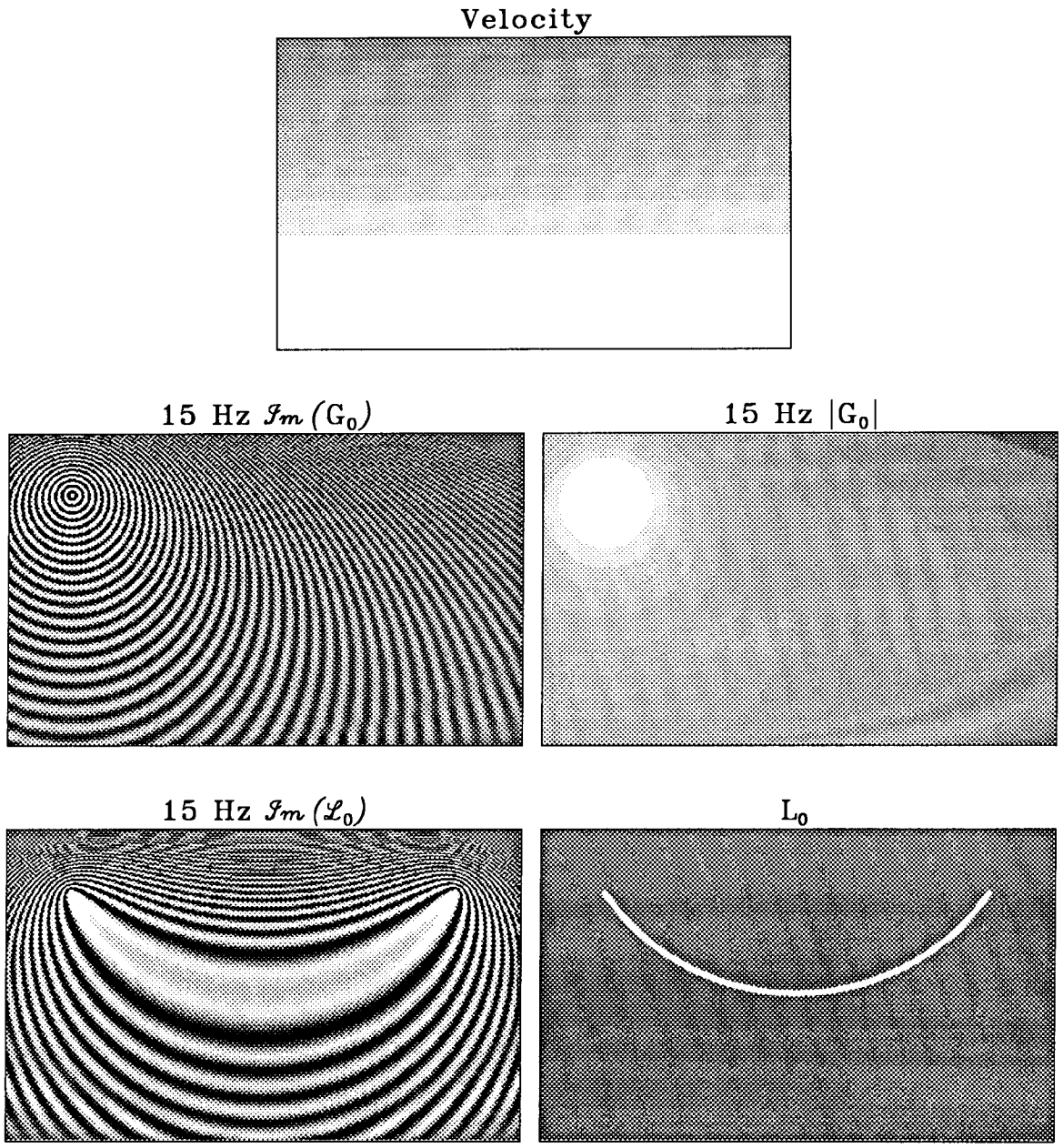

FIG. 3.3. Frequency-space domain wavepath for refraction through a vertical gradient. From top to bottom, left to right: velocity field; 2-d 15 Hz Green's function, imaginary part and modulus; 2-d 15 Hz Rytov wavepath, imaginary part (normalized by $k_0{}^2$); equivalent raypath.

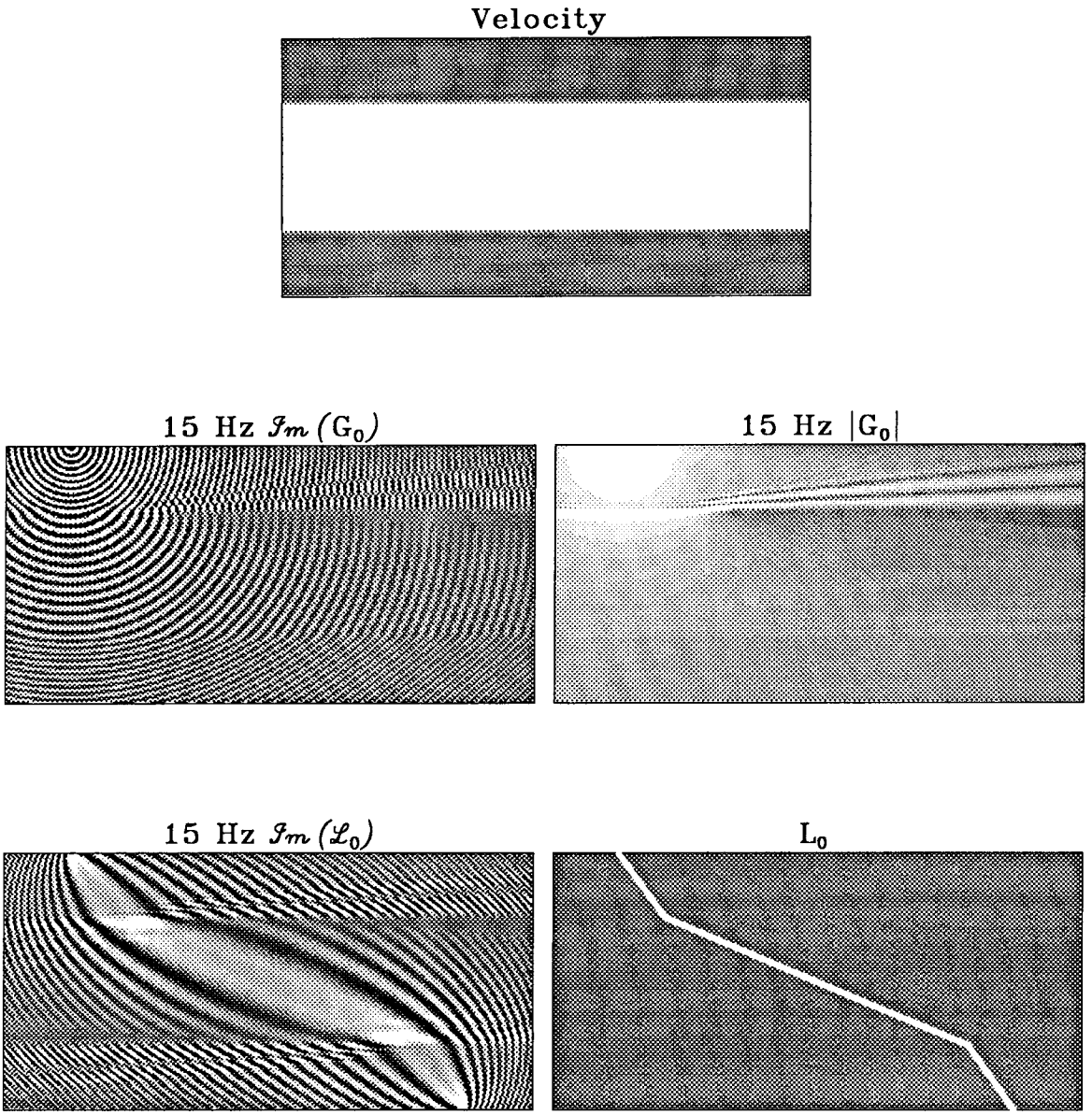

FIG. 3.4. Frequency-space domain wavepath for transmission through layers. From top to bottom, left to right: velocity field; 2-d 15 Hz Green's function, imaginary part and modulus; 2-d 15 Hz Rytov wavepath, imaginary part (normalized by k_0^2); equivalent raypath.

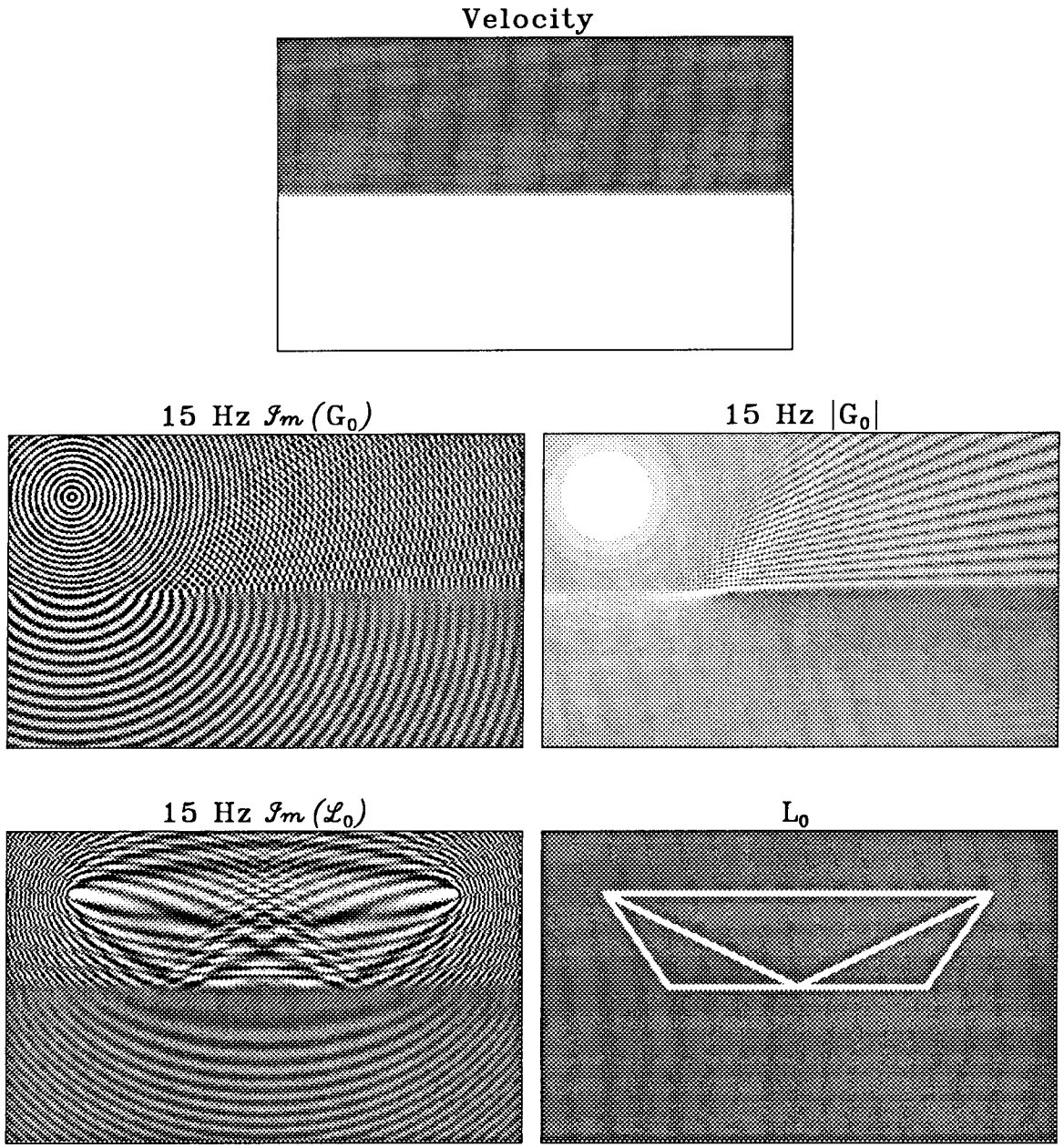

FIG. 3.5. Frequency-space domain wavepath for reflection above an interface. From top to bottom, left to right: velocity field; 2-d 15 Hz Green's function, imaginary part and modulus; 2-d 15 Hz Rytov wavepath, imaginary part (normalized by $k_0{}^2$); equivalent raypaths.

Slices through the transformed cube, $D(x, z, \omega)$, provided the necessary monochromatic Green's functions.

From top to bottom, left to right, the panels in each figure show: the velocity field; the imaginary part of a 15 Hz source Green's function through the field; the complex absolute value of the Green's function; the imaginary part of the corresponding Rytov wavepath, and the equivalent raypath. The examples are limited to imaginary Rytov wavepaths, as these are the backprojection patterns most closely related to raypaths. For the first two transmission geometries, the resulting wavepaths share the same basic features described in the preceding subsection. The imaginary wavepaths appear as elliptical, oscillatory patterns encompassing their corresponding raypaths; they decay in amplitude away from the source and receiver, and their zeroes fall on the Fresnel-zone boundaries. The only new features are the null zones in the layered field's Green's function: appearing both where the direct and post-critically reflected wavefields interfere, and beneath the interface, beyond the critical angle. (The low frequency features at the bottoms and sides of the gradient-field Green's function are artifacts, resulting from imperfect absorbing boundaries.)

The third, reflection geometry example differs somewhat in that it shows multiple, interfering events. Contained in the wavepath are two overlapping elliptical features: a horizontal ellipse describing the direct arrival, and a folded ellipse describing the post-critical, reflection arrival. The weaker, head-wave arrival is not readily apparent. Unlike the previous examples, the zeroes of the imaginary Rytov wavepath no longer fall on the boundaries of the Fresnel zones. The interior regions of the ellipses change sign from frequency to frequency, as determined by interference between the direct, reflected and refracted events. This breakdown in the parallelism between Rytov and ray-trace tomography (and Hagedoorn's beams) occurs when multiple background arrivals are considered simultaneously. This geometry does not fit the transmission-geometry applications for which Rytov tomography is best suited—where cumulative phase delays are proportional to velocity perturbations (Keller, 1969). For this application, the different wavefields would have to be separated before inversion.

For completeness, Figure 3.6 shows time-domain wavepaths for the velocity-gradient and layered-velocity examples of Figures 3.3 and 3.4. An interesting bifurcation appears in the migration patterns, corresponding to the post-critical reflection event. Also faintly visible is the head wave traveling down the layers' interface.

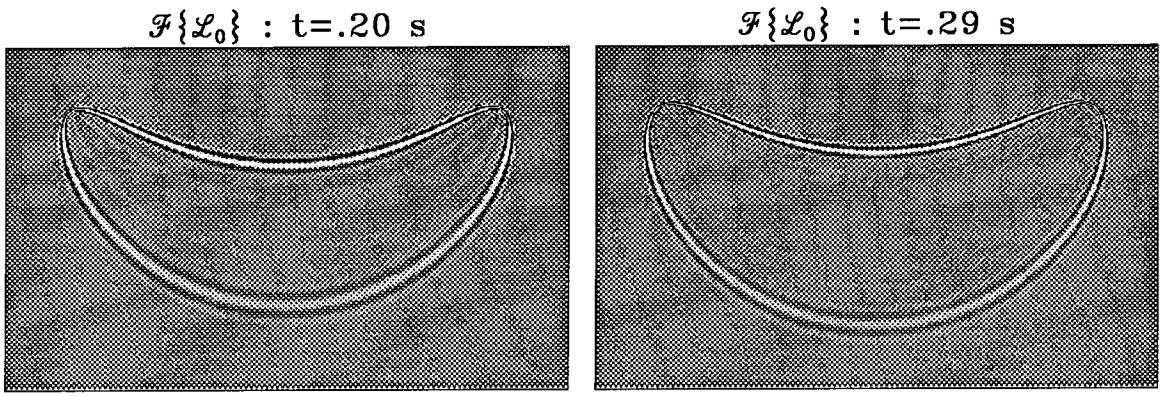

a) Velocity gradient background

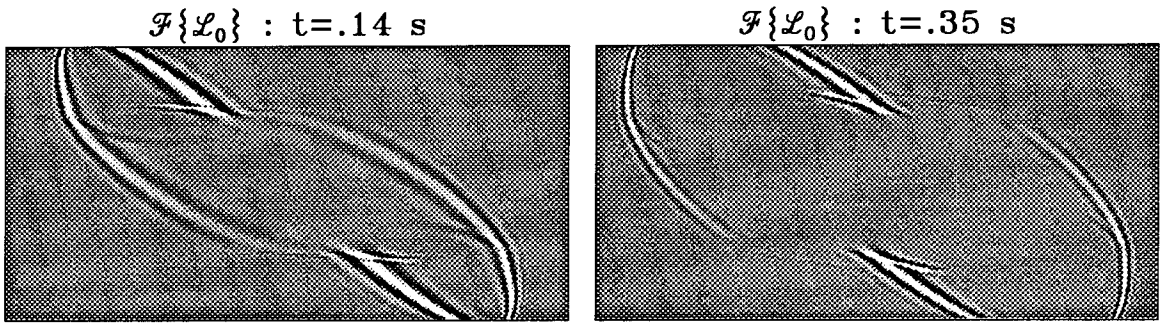

b) Layered velocity background

FIG. 3.6. Time-space domain wavepaths. (a) Velocity-gradient background field. (b) Layered-velocity background field.

3.2 Wavepaths vs. raypaths: space domain

The examples in the preceding section emphasized the similarity between raypaths and wavepaths as tools for visualizing the sampling of a velocity field by a source-receiver experiment—for describing the sensitivity of the experiment to the presence of any velocity perturbation. This section emphasizes their differences.

There are two major distinctions between the raypaths and wavepaths of Figures 3.1, 3.3, 3.4 and 3.5. First, while integration through a velocity field over a raypath yields one measurement for each source-geophone experiment (a traveltime), integration over a wavepath yields an infinite number of measurements (a complex phase or amplitude for each frequency considered). Second, while a raypath interrogates and projects information

back over a small region of the velocity field, a wavepath interrogates and projects information back over the whole field. These differences and the greater information content in wave- as opposed to ray-theoretic tomography arise from the contrasting assumptions the methods make about the seismic experiment.

In theory, the fundamental assumption of ray-trace tomography is one of high frequency: that the spatial wavelength of the seismic source is much smaller than the characteristic dimensions of the velocity field. In practice, for bandlimited seismic data, the assumption is more often one of no geometrical frequency dispersion: that phase delay is approximately linear with frequency and described by an average time delay picked from a wavelet peak. Either way, interpreted through the uncertainty relation, raypaths are compact because ray theory is essentially infinite bandwidth. Behavior over a broad range of frequencies is characterized by a single measurement; scattering is forbidden and energy travels along the fastest source-receiver path.

In contrast to the infinite-bandwidth assumptions of ray-theoretic tomography, wave-theoretic tomography is monochromatic. Well defined in frequency, wavepaths are infinite in extent: capable of modeling scattered energy arriving at any time from any distance. Instead of characterizing a source-geophone experiment by a single time pick, the method considers all the information in the seismic coda. This extra information makes wave-equation tomography far more powerful than ray-trace tomography, but it also makes the method less robust. Where ray-trace tomography inverts traveltime delays for one selected arrival, wave-equation tomography inverts all the energy on a trace simultaneously (direct and scattered arrivals together). For any seismic experiment, the validity of the monochromatic assumption depends on the knowledge of the source, the quality of the data, and whether modeled events can be separated from unmodeled events before inversion. The remainder of this chapter and the synthetic example of the next assume fully monochromatic data. The final chapter returns to this problem and introduces bandlimited raypaths as a tool for hybridizing ray-trace and Rytov wave-equation tomography through the uncertainty relation.

3.3 Wavepaths vs. raypaths: wavenumber domain

One of the advantages of formulating diffraction tomography in the space domain is the capacity it offers for comparing space-domain and wavenumber-domain wavepaths—and

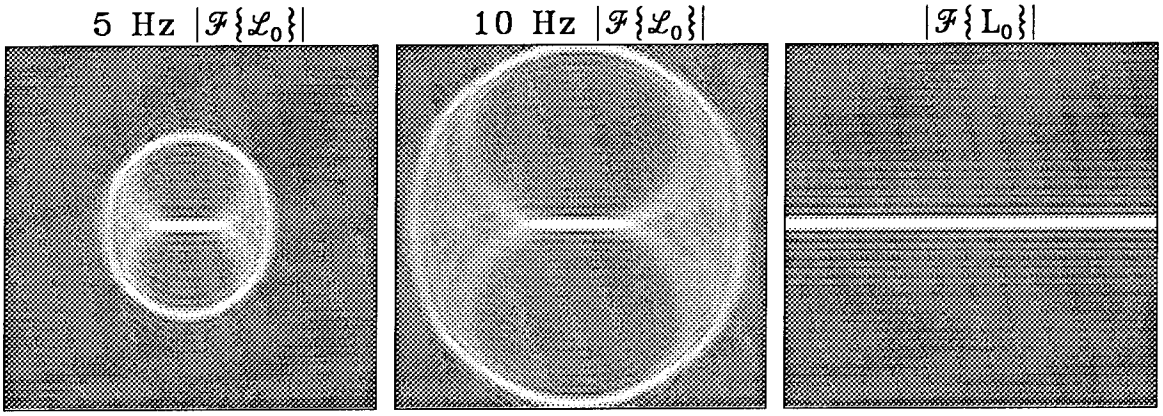

FIG. 3.7. Two-dimensional wavenumber-amplitude spectra. (a) 5 Hz wavepath. (b) 10 Hz wavepath. (c) Raypath. Plots are at the same scale ($k_{max} = 2k_0$, $k_0 = 2\pi \cdot 10/v_0$), origins in the center.

consequently, its linkage of specific spatial regions to specific spectral regions for any source-geophone experiment.

3.3.1 Propagating energy

Figure 3.7 shows the two-dimensional wavenumber-amplitude spectra of the 5 and 10 Hz wavepaths and raypath of Figure 3.1. (The spectra are the same for both the Born and Rytov patterns.) The gross structure of the spectra is easily related to the space-domain patterns: both ray-theoretic and wave-theoretic tomography are most sensitive to spatial frequencies representing velocity variations paralleling the source-geophone axis and least sensitive to those perpendicular to the axis. The fine structure of the wavepath spectra is more difficult to understand.

Devaney (1984) and Wu and Toksöz (1987) show how to construct spectra similar to those in Figure 3.7 from plane-wave scattering arguments. Borrowed from their work, Figure 3.8 illustrates two plane waves: emanating from source **s**, scattering at point **a** or **b**, and arriving at geophone **g**. For source and geophone plane waves described by $\mathbf{k_s}$ and $\mathbf{k_g}$, the scatterer's wavenumber is $\mathbf{k_g} - \mathbf{k_s}$. In plane rectangular coordinates the wavenumber becomes:

$$k_x = 2\frac{\omega}{v}\sin\left(\frac{\alpha_s - \alpha_g}{2}\right)\sin\left(\frac{\alpha_s + \alpha_g}{2}\right)$$
$$k_z = 2\frac{\omega}{v}\sin\left(\frac{\alpha_g - \alpha_s}{2}\right)\cos\left(\frac{\alpha_s + \alpha_g}{2}\right), \qquad (3.2)$$

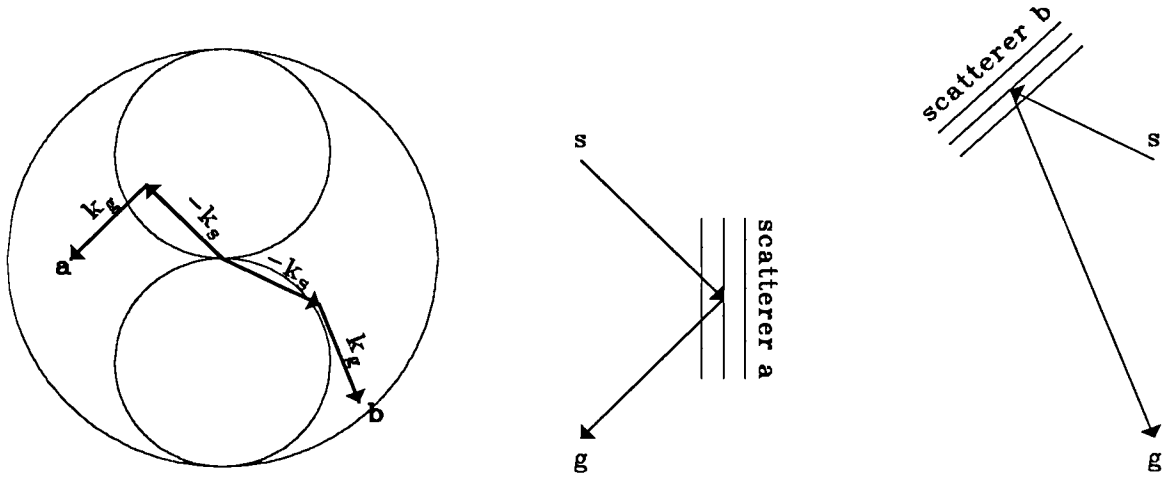

FIG. 3.8. Plane-wave scattering: propagating energy.

where α_s and α_g describe the angles $\mathbf{k_s}$ and $\mathbf{k_g}$ make with the x-axis, respectively. In polar coordinates the wavenumber becomes:

$$\begin{aligned} k_x &= \rho \cos\theta \\ k_z &= \rho \sin\theta, \end{aligned} \tag{3.3}$$

where

$$\begin{aligned} \rho &= 2\frac{\omega}{v} \sin\left(\frac{|\alpha_s - \alpha_g|}{2}\right) \\ \theta &= \frac{\alpha_s + \alpha_g}{2}. \end{aligned} \tag{3.4}$$

For a single source-geophone experiment, the possible combinations of source and receiver plane-wave angles are constrained by the appropriate scattering ellipses. Parameterizing α_g in equation 3.2 in terms of equation 3.1's a and c (the semimajor axis and foci half-offset of a scattering ellipse) produces Figure 3.9. The left and right panels relate the scattering ellipses of Figure 3.1 to the wavepath spectra of Figure 3.7. The wavepath region on the source-receiver axis corresponds to a flat ellipse of eccentricity 1 ($a = 1$) and

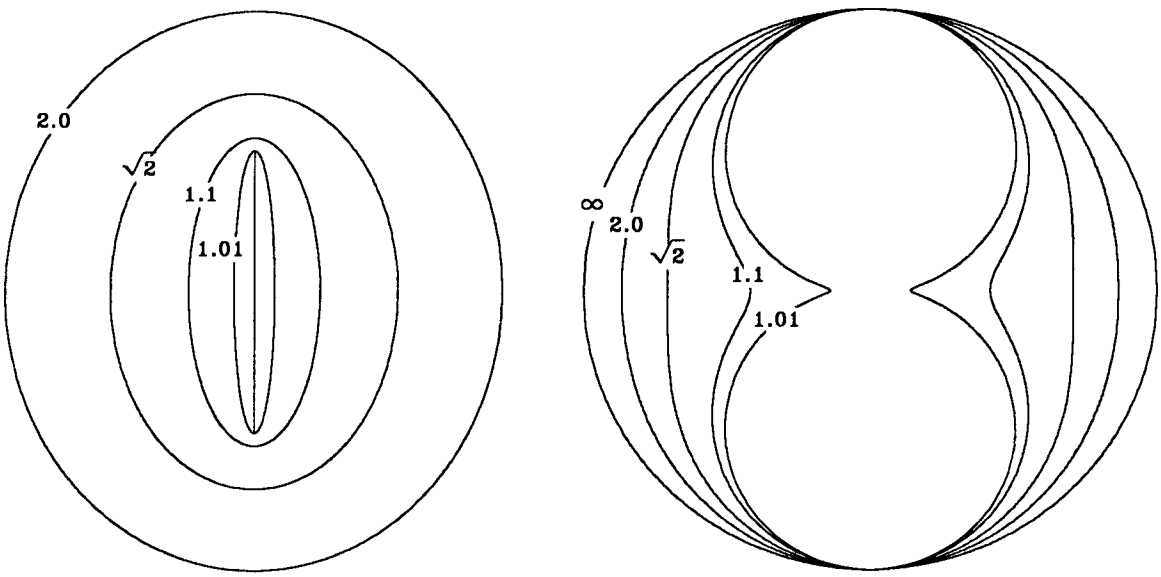

FIG. 3.9. Diagram relating wavepath scattering ellipses to wavepath spatial-amplitude spectra through the semimajor axis parameter a. $a > 1$. (The foci half-offset c equals 1.)

is sensitive to scatterers with wavenumbers outlining the circular holes. The wavepath region surrounding the source-receiver axis corresponds to ellipses of decreasing eccentricity (increasing a) and is sensitive to higher wavenumbers as labeled. The wavepath has a maximum spatial frequency twice that of the source wavefield ($2k_0$), approached as a limit by the spacing of the most distant confocal ellipses. Note that the curve for $a = \sqrt{2}$ encompasses all the scattered arrivals reaching the geophone within 41% of the direct-arrival traveltime.

3.3.2 Evanescent energy

The characteristic holes in the spatial-amplitude spectra of the monochromatic wavepaths arise from a causality (source/sink) condition placed on the source and geophone Green's functions in equations 2.12 and 2.16. Replacing either the source or the geophone Green's function with its complex conjugate yields the wavepaths and spatial-amplitude spectra shown in Figure 3.10. The familiar ellipses (the locus of points the *sum* of whose distances from source and geophone is constant) have been replaced by hyperbolae (the locus of

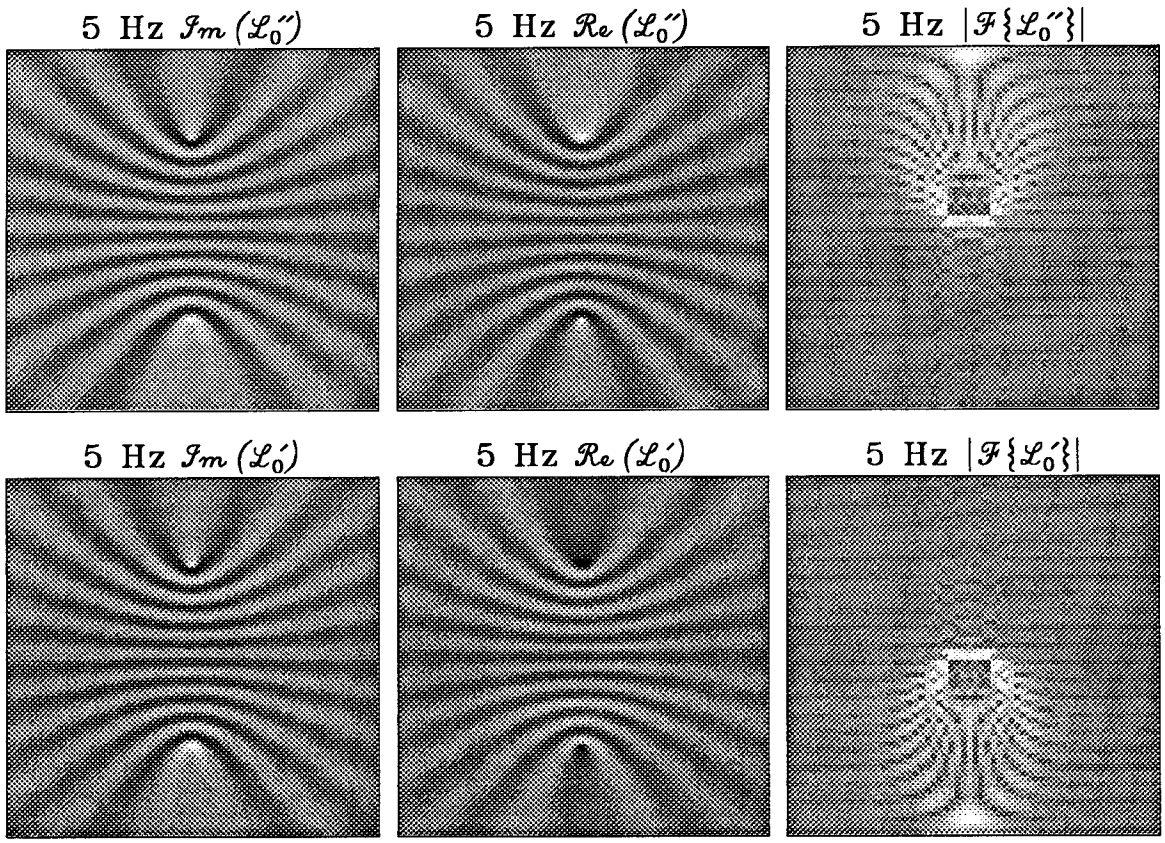

FIG. 3.10. Evanescent energy. Upper plot: monochromatic 5 Hz wavepath and spatial-amplitude spectrum resulting from replacement of the source Green's function in equation 2.9 by $iH_0^{(2)}(k_0|\mathbf{r}|)/4$. Lower plot: monochromatic 5 Hz wavepath and spatial-amplitude spectrum resulting from replacement of the geophone Green's function in equation 2.9 by $iH_0^{(2)}(k_0|\mathbf{r}|)/4$. ($H_0^{(2)}$ is a zero-order Hankel function of the second kind.)

points the *difference* of whose distances from source and geophone is constant):

$$\frac{x^2}{a^2 - c^2} + \frac{z^2}{a^2} = 1; \quad a < c. \tag{3.5}$$

Physically, this transformation results from the replacement of an exploding, causal source by an imploding, anticausal source. Just as energy from an exploding source that is scattered by points along a single ellipse reaches a geophone in phase, energy from an imploding source scattered by points along a single hyperbola reaches a geophone in phase. Alternatively, Figure 3.7 represents propagating energy and Figure 3.10 evanescent energy. Anticausal scattering and the relation between space-domain hyperbolae and wavenumber-domain holes are diagrammed in Figures 3.11 and 3.12.

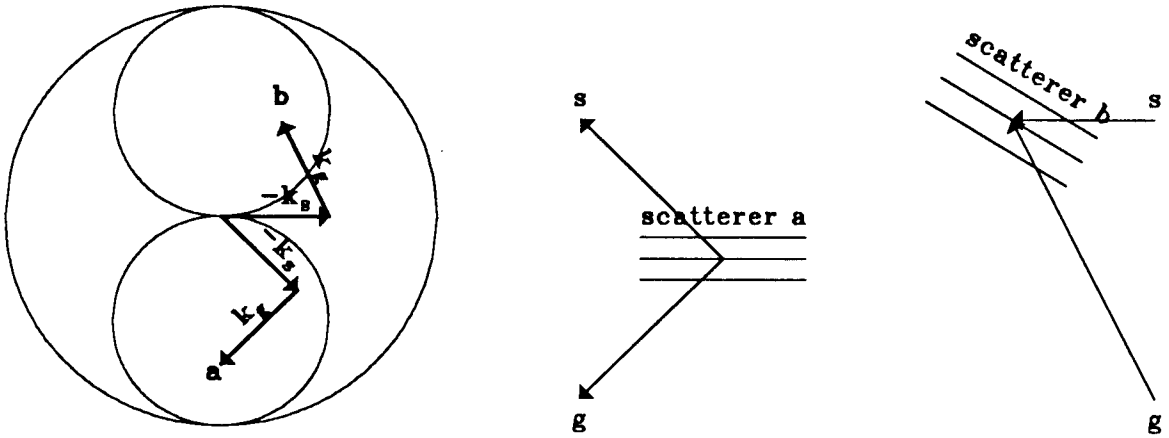

FIG. 3.11. Plane-wave scattering: evanescent energy.

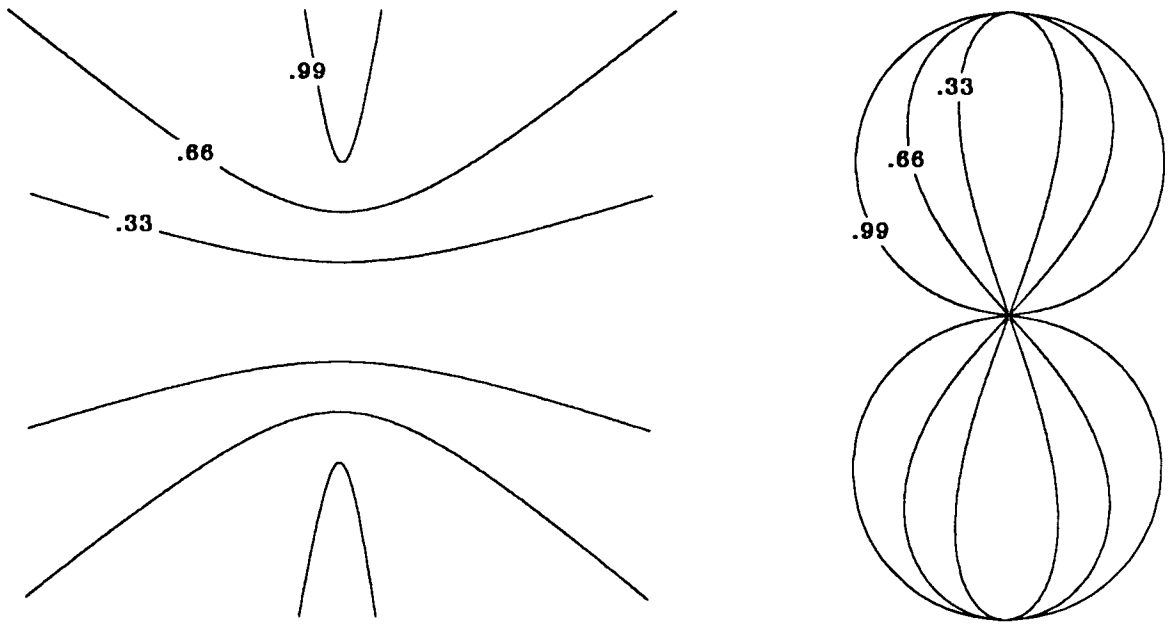

FIG. 3.12. Diagram relating evanescent wavepath scattering ellipses to evanescent wavepath spatial-amplitude spectra through the semimajor axis parameter a. $a < 1$. (The foci half-offset c equals 1.)